Nano Research

ISSN 1998-0124 CN 11-5974/O4
https://doi.org/10.1007/s12274-024-6965-y

Review Article

Colloidal II-VI nanoplatelets for optoelectronic devices: Progress and perspectives

An Hu[1,2], Li Ma[1], Xiaoyu Yang[1,2], Yige Yao[2], Yunke Zhu[2], Jingjing Qiu[2], Shuang Wang[3], Changjun Lu[1] (✉), and Yunan Gao[2,4,5,6] (✉)

[1] *Leyard Optoelectronic Co., Ltd, Beijing 100091, China*
[2] *State Key Laboratory for Artificial Microstructure and Mesoscopic Physics, School of Physics, Peking University, Beijing 100871, China*
[3] *Collaborative Innovation Center of Assessment for Basic Education Quality, Beijing Normal University, Beijing 100875, China*
[4] *Frontiers Science Center for Nano-optoelectronics, Beijing 100871, China*
[5] *Collaborative Innovation Center of Extreme Optics, Shanxi University, Taiyuan 030006, China*
[6] *Peking University Yangtze Delta Institute of Optoelectronics, Nantong 226010, China*

Received: 30 May 2024 / **Revised:** 23 July 2024 / **Accepted:** 12 August 2024

ABSTRACT

Colloidal II-VI nanoplatelets (NPLs) are solution-processable two-dimensional (2D) quantum dots that have vast potential in high-performance optoelectronic applications, including light-emitting diodes, sensors, and lasers. Superior properties, such as ultrapure emission, giant oscillator strength transition, and directional dipoles, have been demonstrated in these NPLs, which can improve the efficiency of light-emitting diodes and lower the threshold of lasers. In this review, we present an overview of the current progress and propose perspectives on the most well-studied II-VI NPLs that are suitable for the optoelectronic applications. We emphasize that the control of the symmetrical shell growth of NPLs is critical for the practical utilization of the advantages of NPLs in these devices.

KEYWORDS

nanoplatelets, quantum wells, colloidal quantum dots, light-emitting diodes

1 Introduction

Colloidal II-VI nanoplatelets (NPLs), also known as quantum wells or nanosheets, are a class of colloidal quantum dots (QDs) with asymmetrical morphology [1–3]. For the discovery and synthesis of QDs, scientists Moungi Bawendi, Louis Brus, and Alexei Ekimov were awarded the 2023 Noble Prize in Chemistry [4]. Utilizing the quantum confinement effect, QDs exhibit optoelectrical properties related to morphology, thereby allowing researchers to control the confinement strength by altering the size. The confinement strength, quantified by the confinement energy $E_{confine}$, is inversely proportional to $m_{eh}R^2$, where m_{eh} is the effective mass of excitons and the R is the size of QDs. The confinement energy can elevate the energy of excitons and emitted photons, which are radiated by a process known as exciton recombination. Consequently, a wide range of size-tunable emission and absorption can be realized, across the ultraviolet, visible, and infrared spectra. The energy elevation is quantized, which inhibits thermal depopulation of the band-edge levels and reduces the lasing thresholds compared to bulk materials [5]. The uniformity of confinement between QDs is guaranteed by the high degree of size uniformity, allowing pure emissions as evidenced by the full-width-at-half-maximums (FWHMs) down to ~ 10 nm and identical emissions from a single dot and from the ensemble of dots [6, 7]. This pure and continuously tunable emission of QDs fills the deficiencies of traditional semiconductors. Furthermore, with the solution processability and high compatibility gained from the colloidal system, QDs are highly prized in optoelectronic devices such as light-emitting diodes (LEDs) [8] and lasers [9].

In addition to controlling the strength of the quantum confinement, researchers can also control the symmetry of the confinement by altering the shape of QDs. QDs with a symmetrical spherical shape thus possess symmetrical quantum confinement, where the strength of confinement along each direction is nearly equal, as illustrated in Fig. 1(a). Comparably, NPLs possess a platelet shape and asymmetrical quantum confinement where the strength of confinement along one direction is strong, as shown in Fig. 1(b). This direction is often referred to the vertical direction or Z-direction and the other two directions along which the confinement is weak are called the lateral directions. The asymmetrical morphology of NPLs results in distinctive optoelectronic properties, which can be advantageous in applications.

The optoelectronic properties of NPLs are largely determined by the thickness and crystal structures, which require elaboration. The crystal structures of NPLs can be divided into two categories: cubic zinc-blende and hexagonal wurtzite crystal structures. The thickness of NPLs is usually indicated by the number of chalcogen and metal monolayers (MLs). For N MLs zinc-blende NPLs, N MLs of chalcogen and $N + 1$ MLs of metal are alternately stacked along the [001] polar direction and terminated with metal layers

Address correspondence to Changjun Lu, luchangjun@leyard.com; Yunan Gao, gyn@pku.edu.cn

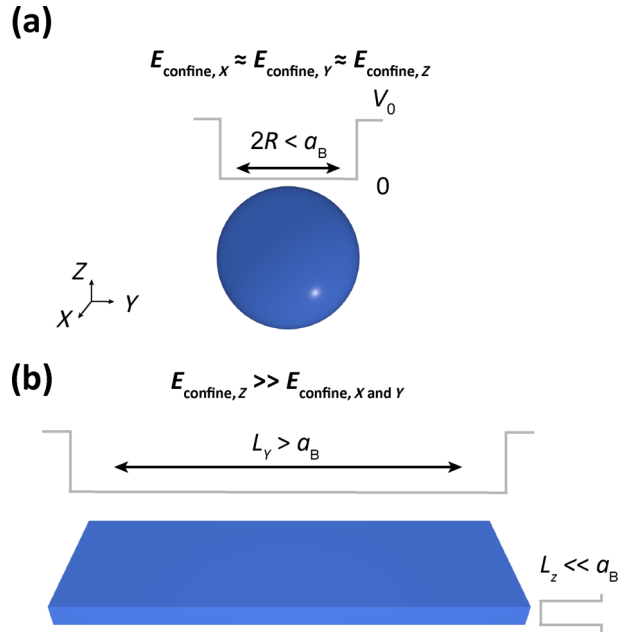

Figure 1 Illustration of the morphology-tailored quantum confinement for (a) spherical QDs and (b) NPLs. The height of the confinement potential is V_0. In spherical QDs, the confinement is symmetrical, and the strength of the confinement is determined by the radius R of QDs and the Bohr radius α_B of excitons. In NPLs, the confinement is asymmetrical, with the weak confinement along the X and Y axes and the strong confinement along the Z axis due to the length L_Y larger than α_B and thickness L_Z smaller than α_B.

[10]. In addition, N MLs wurtzite NPLs are stacked along the $[11\bar{2}0]$ non-polar direction [1].

This review presents the current progress and proposes perspectives on colloidal II-VI NPLs, as they represent the most extensively studied branch of NPLs. Previous reviews of NPLs have comprehensively detailed the ligands, synthesis, origin of asymmetry, optical properties, optoelectronic integration, and heterostructures [10–14]. It is argued here that the control of shell growth is critical to minimize the gap between theoretical advantages of NPLs and practical performance of NPL devices. We begin with an introduction to the advantages of NPLs and the challenges of NPLs for achieving high-performance devices. With the aim to induce symmetrical shell growth around NPLs, we then summarize the current progress in achieving such NPLs, including the formation mechanisms, morphology regulation, and heterostructures of NPLs. After that, we review the progress in assembling NPLs to utilize the NPL advantages in devices. In the last section, we give perspectives on NPLs for devices.

2 Advantages of NPLs for devices

The advantages of NPLs center at minimizing energy loss for various devices and, according to the properties of NPLs, can be summarized as fourfold: the atomically uniform surface, the large light-heavy hole splitting, the giant oscillator strength (GOST), and the directional dipoles. NPLs exhibit atomically tunable and atomically uniform sizes, which enables researchers to tune the precision and uniformity of the confinement potentials. For example, zinc-blende CdSe NPLs is atomically uniform even in the ensemble of NPLs, resulting in FWHMs down to 7 nm, as shown in Fig. 2(a). Such a highly tunable and uniform morphology in an ensemble has the advantage of practically realizing the orders-of-magnitude minimum of the non-radiative Auger rate, which is easily averaged out by the size variation of the QDs [15], as shown in Fig. 2(b). This size-related oscillation of Auger processes has been utilized to interpret the experimentally discovered nonmonotonic dependence of the Auger process on the shell thickness in core/shell NPLs [16], as shown in Fig. 2(c) and 2(d). Furthermore, it is found that the Auger lifetime also depends on the lateral size A of NPLs. The dependence is linear [17, 18], in the regime $A \leq 100$ nm^2, and plateau [19], in the $A \geq 150$ nm^2. Atomistic and electronic structure-based calculations of Auger lifetime show the electrons and holes delocalize over the entire NPL with the $A = 64$ nm^2, yielding the lateral-dependent Auger process. While similar calculations are unfeasible for $A \geq 150$ nm^2 due to the complexity, one could assume that the lateral quantum confinement is negligible so that the initial bi-excitonic state does not change when the lateral size is larger than the biexciton Bohr radius [19]. Therefore, we conjecture that the possible averaging effect of Auger processes resulting from the variations in lateral sizes may be minimized by increasing the lateral size, allowing the impact of uniform thickness to be independently studied.

Another advantage of NPLs is the large light-heavy hole splitting, which lifts the degeneracy of band-edge holes. The lifted degeneracy of holes can lower the threshold number of excitons per dot $\langle N_{th,gain} \rangle$ required for the optical gain in lasing. The optical gain requires the population inversion conditions in the sample and is related to the degeneracy of band-edge electrons g_e and holes g_h as $\langle N_{th,gain} \rangle = g_e g_h / (g_e + g_h)$. In QDs, the degeneracy of band-edge electrons and holes is 2 and 4, respectively, yielding a $\langle N_{th,gain} \rangle = 1.3$. If the hole state is lifted by the light-heavy hole splitting larger than $k_B T$, the hole degeneracy is reduced to 2, yielding a $\langle N_{th,gain} \rangle = 1$. While the crystal structure and shape anisotropy in QDs can lift the hole degeneracy, the effect is still comparable to thermal fluctuation, as shown in Fig. 3(a). To lift the hole degeneracy, asymmetrical QDs with biaxial strain are synthesized. The asymmetrical QDs demonstrate a light-heavy hole splitting around 54 meV. This value is further increased to around 100 meV in NPLs, with a high asymmetrical morphology, as evidenced by the absorption spectra of CdSe core and CdSe/CdS core/shell NPLs, as shown in Fig. 3(b) [16, 20]. In addition, the large light-heavy hole splitting can also suppress the self-absorption effect.

NPLs exhibit the GOST effect, a quantifier of the light-matter interaction, originating from the enhanced overlapping between the ground and the excited states. It is proposed that the GOST of NPLs is the sum of multiple and low oscillator transitions [21]. The thermal energy at room temperature and the crystal defects are sufficient to decohere and localize exciton and lower the oscillator transitions. Nevertheless, the oscillator strength deduced from the linear absorption spectrum suggests that the overall strength is proportional to the volume of the NPLs [21, 22]. Therefore, we can obtain a large absorption cross-section, by expanding NPLs along lateral directions, as shown in Fig. 3(c). For example, a typical absorption cross-section of QDs with a thick composition-graded shell (cg-shell) is 1.80×10^{-13} cm^2 at 400 nm, while the value of NPLs reaches 5.06×10^{-13} cm^2, suggesting that NPLs are excellent concentrators for photons and electrons [20, 23, 24]. This property implies that the volume ratio between NPLs and ligands, which are transparent to light and are insulators to current, can be minimized. As a result, NPLs with a large absorption cross-section can improve the performance of optoelectronic devices, such as luminescent solar concentrators with increased output power [23], color conversion filters with a thinner thickness [25], and electrical devices with a decreased Joule loss [26].

Moreover, NPLs have the potential to improve the efficiency of devices that adopt planar structures with an emitting layer sandwiched by high refractive index materials and mental layers. The electrons and holes are transported to the emitting layer where NPLs can absorb electrons and holes and form excitons. It

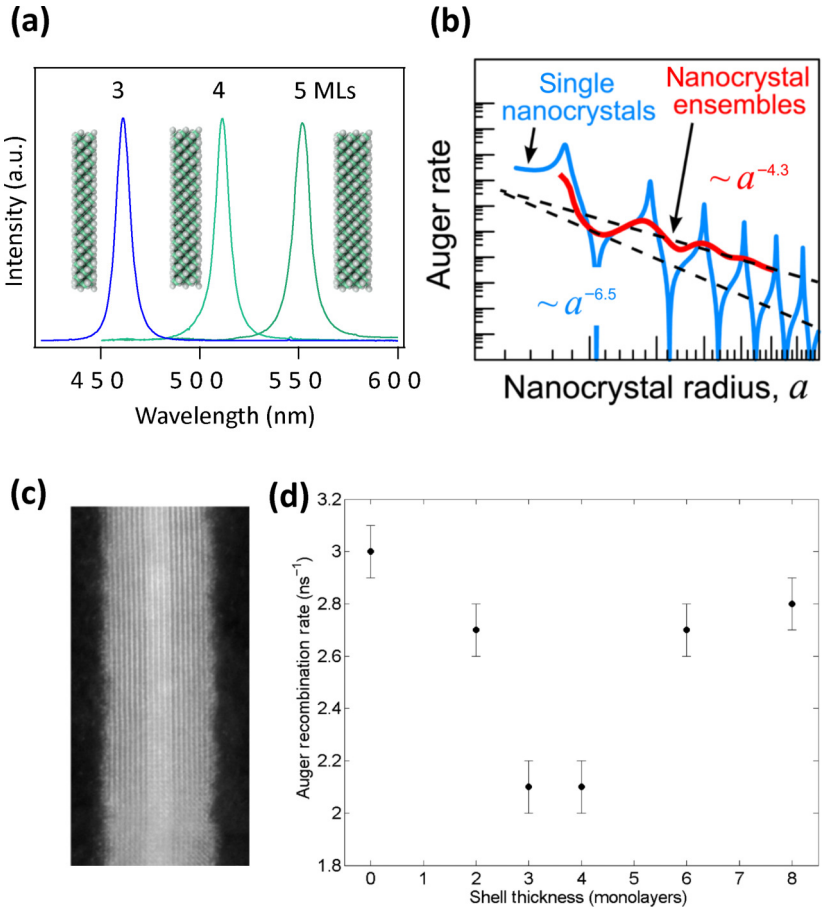

Figure 2 (a) The emission spectra and corresponding structure illustration of zinc-blende CdSe NPLs with different thickness. (b) Size dependence of the nonradiative Auger recombination rate calculated for negative trions in single and ensemble CdSe QDs. Reproduced with permission from Ref. [15], © American Chemical Society 2015. (c) Cross-sectional dark-field TEM image of a core/shell NPL with 4 ML CdSe and 6 ML CdS. (d) Auger recombination rate as a function of the shell thickness for CdSe/CdS core/shell NPLs with 4 ML CdSe core. Reproduced with permission from Ref. [16], © American Chemical Society 2017.

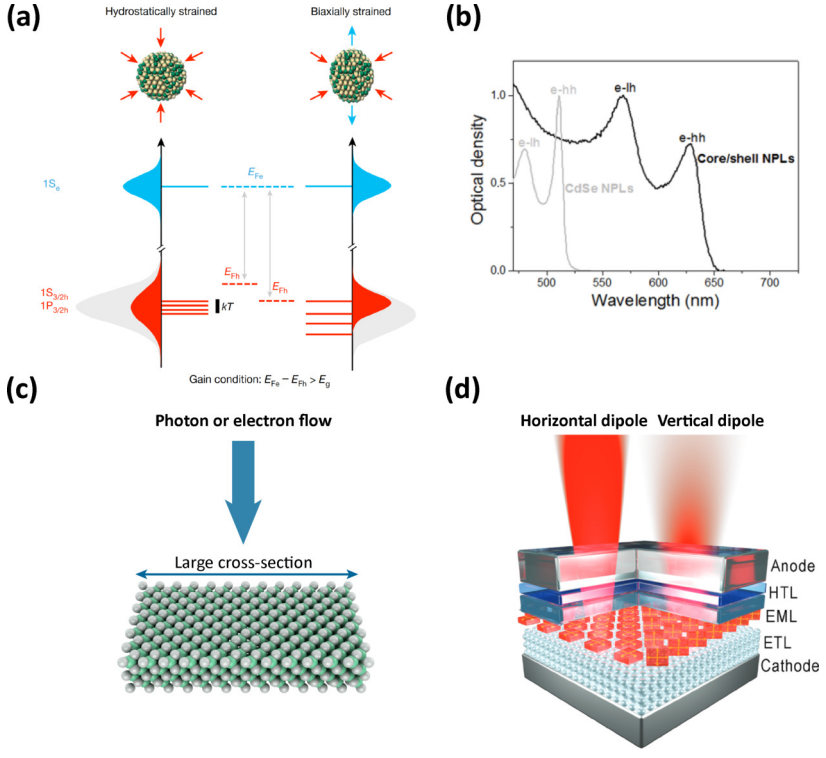

Figure 3 (a) Illustration of band-edge states, state filling and the quasi-Fermi-level splitting under hydrostatic and biaxial strain in CdSe QDs, where the red and blue arrows denote the presence and absence of compressive strain, respectively. The biaxial strain enlarges the light-heavy hole splitting to exceed the thermal energy *kT*. Reproduced with permission from Ref. [32], © Macmillan Publishers Limited, part of Springer Nature 2017. (b) Illustration of the strong biaxial strain and absorption spectra of CdSe NPLs and CdSe/CdS core/shell NPLs. Reproduced with permission from Ref. [33], © American Chemical Society 2013. (c) Illustration of the large cross-section of NPLs. (d) Illustration of the NPL LEDs with enhanced external quantum efficiency. Reproduced with permission from Ref. [34], © Wiley-VCH GmbH 2023.

has been shown that while the NPL transition dipoles is isotropic during absorbing carriers, these dipoles are aligned in the NPL plane during emitting [27]. These in-plane dipoles are attributed to the in-plane dipole moment, the optical density of states, and the local electric field renormalized by the dielectric contrast between the NPLs and the surrounding medium [28, 29]. Critically, in devices with the planar structure, a substantial portion of the emitted energy is attributed to the horizontally aligned dipoles not vertically aligned dipoles. This is partly because vertical dipoles emit light in transverse magnetic mode, which is absorbed by the metal layer, and partly because most emitted light is outside the angle of total internal reflection. Therefore, once 100% dipoles are aligned horizontally in devices, NPLs allow an estimated 50% increase in overall device efficiency compared to that of QDs with 67% horizontally aligned dipoles. Recently, this enhancement has been realized through systematical engineering on the heterostructure and assembly of NPLs, as shown in Fig. 3(d). Besides, NPLs can also emit polarized lights, which presents a potential for three-dimensional (3D) imaging [30, 31].

To fully leverage these advantages of NPLs in various optoelectronic devices, we should suppress non-radiative processes within NPLs and orient NPLs within devices, warranting the investigation of the synthesis and assembly of NPLs.

3 Challenges of NPLs for devices

The nano size of NPLs facilitates fascinating optoelectrical properties, yet simultaneously leads to the non-radiative processes that deteriorate the performance of NPLs. Non-radiative processes, mostly leading to thermal dissipation, indicate that the energy of excitons is not transferred to emitted photons, but rather to other particles [35]. The energy can be transferred non-radiatively among NPLs, as shown in Fig. 4(a), and within NPLs, but the more important processes are the latter ones. This is because when energy transfers among NPLs, non-radiative NPLs lose the energy within these NPLs and cease the transfer. The energy transfer rate among NPLs is proportional to d^{-4}, where d is the distance between NPLs [36, 37], implying it can be addressed by simply increasing the distance among NPLs. However, the suppression of non-radiative processes within NPLs is one of the significant challenges for the high-performance devices. We will revisit the progress made in QDs and QD devices, where this problem has been well addressed, and then propose the symmetrical shell growth can solve the challenges of NPLs for devices.

3.1 Insights from QDs

The phenomenon of trapping by surface defects arises from the high surface-to-volume ratio of QDs. Due to the large surface area, excitons within QDs are sensitive to un-passivated surface atoms and molecules. To alleviate this sensitivity, researchers have devised the growth of high bandgap materials around QDs, to form core/shell heterostructures [38], where the shell can create a spatial distance and energic potential between excitons, localized mainly within the core, and surface traps, localized at the surface of the shell [39], as shown in Fig. 4(b). In this context, we focus on the type-I heterostructure, since a potential barrier can be established for electrons and holes inside the core. For instance, in the CdSe/CdS heterostructure, the energetic offsets for valence and conduction band are 0.39 and 0.18 eV, respectively.

The growth of the shell, if not well controlled, induces lattice defects at the core-shell interface or within the shell [40]. Research shows that the suppression of interface defects could be effectively achieved by implementing gradient composition [41]. Additionally, slow and high-temperature growth could also alleviate the lattice mismatch [38, 42]. The stacking faults within the shell, caused by the steric hindrance between bulky ligands, can be reduced by detaching bulky ligands [43]. The passivation of surface and lattice defects assists the realization of QDs with outstanding optical properties, such as near-unity photoluminescence quantum yields (PLQYs) and non-blinking properties at the single dot level [44, 45]. These QDs are desirable in applications operating at low exciton density, such as luminescent solar concentrators [46], sensing and imaging [47, 48], and photon down conversion at low intensity [25].

In devices operating at high exciton density where multibody dynamic dominates, including LEDs which commonly operate under the electron-rich environments, and lasers which commonly operate under the multi-exciton environments, the Auger process shrinks the LED lifetime and surges the lasing threshold [50–52]. The fast Auger process in QDs originates from the strong confinement effect, which enhances the Coulomb

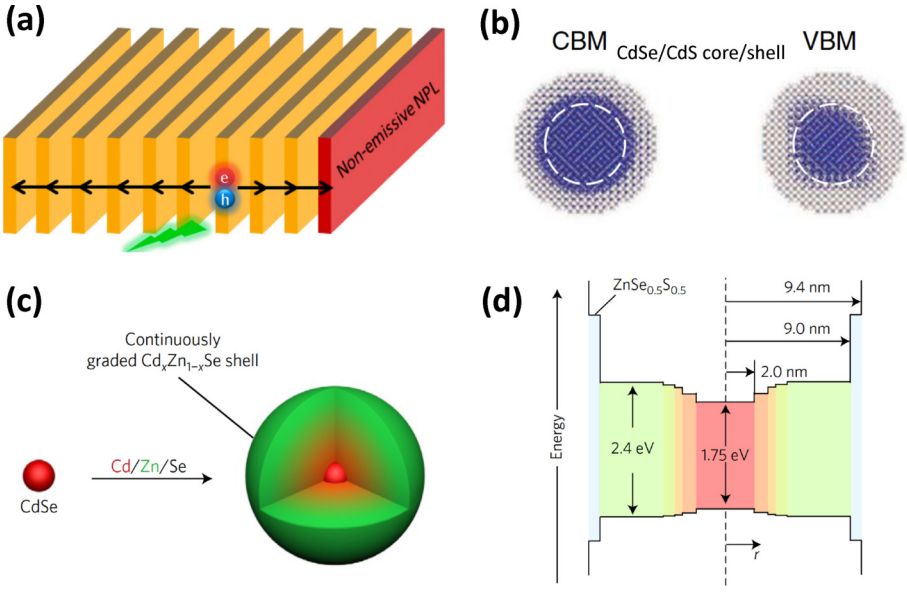

Figure 4 (a) Illustration of energy transfer among NPLs. Reproduced with permission from Ref. [37], © American Chemical Society 2014. (b) The theoretical charge density results of the conduction band minimum (CBM) and valence band maximum (VBM) for CdSe/CdS core/shell QDs. Reproduced with permission from Ref. [39], © Hou, X. Q. et al. 2019. (c) The synthesis procedure and (d) the electronic structure of the continuously graded shell. Reproduced with permission from Ref. [49], © Springer Nature Limited 2017.

interaction and relaxes the momentum conservation rule. Theoretically, engineering the confinement effect, such as increasing the width of confinement and smoothening the potential of confinement, has been explored as an efficient method that mitigate the Auger process [53, 54]. Moreover, the widening and smoothening of the confinement is synthetically realized by growing a cg-shell [41, 49], which boosts the Auger lifetime to nanoseconds from hundreds of picoseconds, as shown in Figs. 4(c) and 4(d). The cg-shell can also facilitate the charge transportation and mitigate interface traps. These Auger-suppressed QDs enable long-lifetime QD LEDs [51, 55] and electrically driven QD lasers [9], which signifies a leap forward in the field.

3.2 NPL's structural design for devices

The advancement of QDs has demonstrated that shell growth is the dominator factor in the suppression of various non-radiative processes. The shell growth for QDs is often presumed to be symmetrical, due to the symmetrical morphology of spherical QDs. However, when asymmetrical NPLs are of concern, the symmetry of shell growth cannot be guaranteed. Indeed, the very existence of NPLs implies a contradiction to the symmetrical growth, where the vertical growth is suppressed and lateral growth permitted. The suppressed vertical growth denotes insufficient suppression of various non-radiative processes along that direction and an abrupt potential interface that impedes charge transportation.

The NPL-LEDs are one of the most important devices of NPLs, where they are expected to surpass QD-LEDs by facilitating the advantages of NPLs [56]. The realization of high-performance NPL-LEDs relies on the development of device structures and of device-suitable NPLs. The device structure is at intensive investigations and is similar to that the QD-LEDs [13, 57, 58], and thus we narrow the scope to the development of device-suitable NPLs.

The NPL's design for device is related to the heterostructure, more specifically to the growth of dissimilar materials. In the absence of a heterostructure, the core-only NPL-LEDs display external quantum efficiencies (EQEs) dramatically below 1% [59]. There are also factors that may be responsible for the poor performance, such as the surface defects and the accelerated quenching in the NPL film [37, 60, 61]. These factors are well addressed by the utilization of core/crown NPLs, where dissimilar materials are laterally grown. The edge defects, prominent defects in NPLs [62], can be well passivated by the crown and the quenching in the film could be alleviated by the regulation of core size [63, 64]. However, the performance of core/crown LEDs is still unsatisfactory, presenting EQEs below 10% and instability under high voltage and long operation time [63–67]. Finally, the core/shell heterostructure where dissimilar materials are isotropically grown may provide enhanced stability, effective defect suppression, and balanced charge transport. Coupled with the optimization of device structure, the EQEs of core/shell NPLs are incrementally increased from 0.63% to above 20% by designing and synthesizing novel shell [34, 68–73], such as gradient shell.

Therefore, to realize device-suitable NPLs, it is necessary to induce the shell growth both vertically and laterally while smoothing confinement potentials with a composition gradient. Hence, it is essential to understand the underlying reasons behind the suppression of the vertical growth, the methods for regulating both vertical and lateral growth, and the techniques for controlling the composition. These topics will be introduced and discussed in the following sections, regarding the formation mechanisms, the morphology regulation, and the heterostructures of NPLs.

4 Progress of realizing NPLs suitable for devices

4.1 Formation mechanisms of NPLs

The formation mechanisms of NPLs may provide the insights to regulate the vertical growth, allowing researchers to first halt the vertical growth to form NPLs and then activate it to form a symmetrical shell. The formation mechanisms of NPLs differ for wurtzite and zinc-blende crystal structures. CdSe wurtzite NPLs has been first synthesized in 2006 [1]. To account for the asymmetrical morphology of wurtzite NPLs, two-dimensional (2D) lamellae template theory has been hypothesized [1, 74–79]. This theory proposes that the 2D metal-amine compound presupposes a layered structure that guides the growth of NPLs. However, it is experimentally observed that the Zn-amine lamellae template completely disappear and transform into a disordered state when the temperature is above 60 °C [80]. For the Cd-carboxylate, the polymorphic transition is observed around 100 °C, but a disordered state is then observed when the temperature reaches 180 °C and remains when the temperature drops to 25 °C, indicating the absence of template [81]. Therefore, NPLs synthesized under high temperatures needs further investigation [75, 82].

To further rationalize the formation of these NPLs, research has focused on facet properties, particularly on the reactivity or geometry size of facets. The high reactivity of facets allows a high energy gain when the facet grows, and the surface energy could be obtained by the first-principles calculations. For example, wurtzite NPLs are usually reported with thickness of 8 monolayers along $[11\bar{2}0]$ direction, including NPLs synthesized with various components such as CdSe [74, 83], ZnSe [84, 85], and CdTe [86]. The first-principles calculations indicate that further deposition of an additional atomic layer along the $[11\bar{2}0]$ direction is inaccessible because the formation energy reaches 0.0654 eV, far beyond the experimental conditions [85]. On the other hand, along [0001] and $[1\bar{1}00]$ directions, wurtzite NPLs can grow through the monomer diffusion and reconstruction or the oriented attachment. The oriented attachment refers to fusion of adjacent nanocrystals and the calculation shows the formation energy of fusion along $[1\bar{1}00]$ direction reaches −7.1 eV, which explains the fast lateral growth of wurtzite ZnSe NPLs.

The oriented attachment is also proposed to explain the asymmetrical morphology of zinc-blende NPLs. Zinc-blende CdSe NPLs, for example, are typically synthesized by heating a mixture of long-chain cadmium carboxylate and element selenium in a non-coordinating solvent, after which the short-chain cadmium carboxylate is introduced. In the formation of zinc-blende 5 ML CdSe NPLs, this theory suggests that {100} planes are stabilized by the long-chain ligands while {110} facets are activated by the short-chain ligands, causing the fusion of adjacent nanocrystals along {110} planes [87]. The oriented attachment theory can be used to explain the formation of wurtzite NPLs [85]. However, the oriented attachment theory for CdSe zinc-blende NPLs is not consistent with tests utilizing time-resolved X-ray scattering, which demonstrates a continuous attachment of monomers.

The geometry size of facets provides an alternative perspective to the explanation of the asymmetrical morphology [81], as shown in Fig. 5(a). According to the classical nucleation and expansion theory, the nucleation barrier is the energy required for a new island to form on a facet. The island must reach a critical size so that the expansion of the island is thermodynamically favorable. When the sizes of all facets are much larger than the critical size, as in the case of bulk materials, the growth is independent of the facet sizes and is therefore symmetrical. When the width of facets is decreased below the critical size, as in the case of nanocrystals with narrow facets, a notable decrease in the nucleation barrier

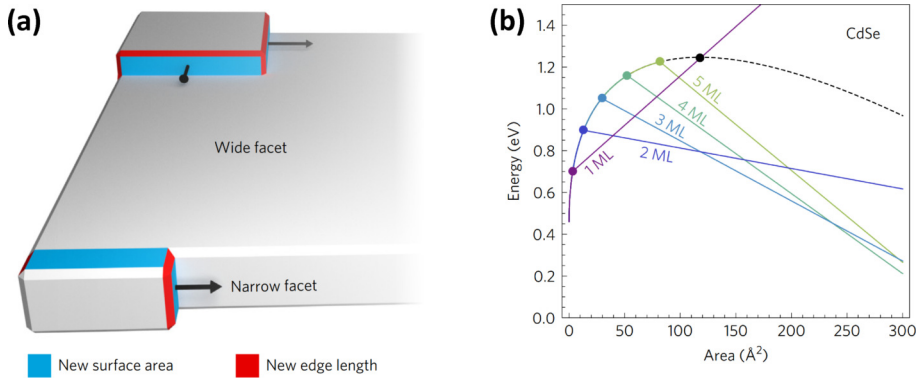

Figure 5 (a) Illustration of asymmetry related to the geometry of facet. (b) Calculated energy related to island size on wide (black dash line) and narrow (color line) facets of CdSe NPLs with different thickness. Reproduced with permission from Ref. [81], © Springer Nature Limited 2017.

occurs, thus explaining the fast growth on narrow facets and the slow growth on wide facets that is larger than the critical size, as shown in Fig. 5(b). Quantitatively, an increment of 0.3 eV in the nucleation energy results in 1000 times decrease in the growth rate. This suggests a kinetic instability regarding the size of facets, which suggests that NPLs can evolve from random fluctuations of cubical seeds. The formation of 2–9 MLs zinc-blende CdSe NPLs, along with the formation of CdS, CdTe, FeS_2, and $CsPbBr_3$ NPLs, can be explained by this intrinsic kinetic instability.

It is noteworthy that the facet-related asymmetry is contingent upon the premise that the rate-determining step of the growth is not the isotropic diffusion process of monomers, which is typically observed in the solution environments [81]. Solvent-free experiments that create an environment with high concentrations of monomers show both long- and short-chain cadmium carboxylate can lead to the formation of NPLs. This result implies that the combination of long-chain and short-chain cadmium carboxylate in a typical synthesis of CdSe NPLs drives a phase separation that transfers the diffusion-limited growth to island-nucleation-limited growth, which relates to facet properties. Therefore, we conjure that a method of regulating the vertical growth of zinc-blende NPLs lies in this premise: vertical growth can be first suppressed by creating a high monomer concentration and then be activated by lowering it, along with increasing temperature or precursor reactivity.

4.2 Morphology regulation of NPLs

Along with advances in mechanism investigations, synthetic insights are deepened by the investigation of precursors, enabling researchers to practically regulate the morphology of NPLs. This is accomplished by regulating the morphology of zinc-blende CdSe NPLs which can be classified into vertical and lateral regulation, where the former focuses on synthesizing thick NPLs and the latter on controlling lateral sizes of NPLs.

For the vertical regulation as shown in Fig. 6(a), the typical synthesis method of zinc-blende CdSe NPLs could only yield NPLs with thickness below 6 MLs. As predicted by the NPL formation theory, m ML NPLs are stable under the conditions $[2E_A/(|E_V|/L)] < m$, where E_A and E_V are energies per unit area and volume, respectively, and L is the height of one monolayer [81]. The obtainable thickness can be expanded by minimizing the E_A, which is synthetically demonstrated by the addition of strongly

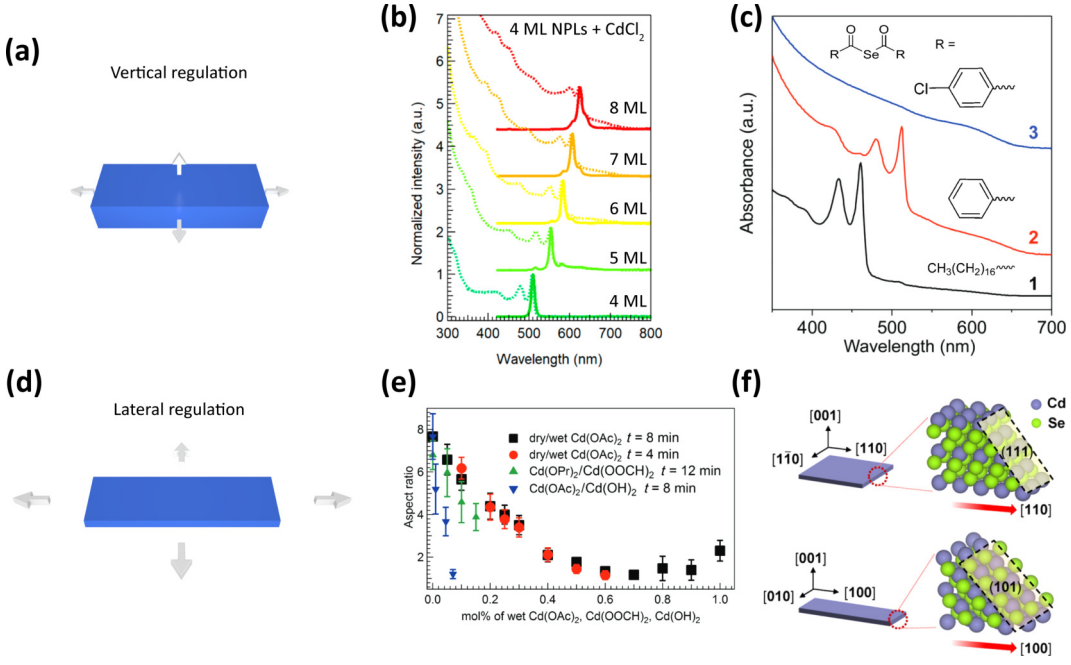

Figure 6 (a) Illustration of the vertical regulation on NPLs. (b) Absorption and emission spectra of NPLs with enhanced growth rate of basal facets by the addition of cadmium chloride. Reproduced with permission from Ref. [88], © American Chemical Society 2018. (c) Absorption spectra of NPLs with different thickness obtained by different selenium precursors. Reproduced with permission from Ref. [91], © The Royal Society of Chemistry 2018. (d) Illustration of the lateral regulation on NPLs. (e) Plot of the CdSe NPL aspect ratio versus molar percentage of different cadmium precursors. Reproduced with permission from Ref. [92], © The Royal Society of Chemistry 2016. (f) Illustration of the lateral growth direction of NPLs with different lateral shapes. Reproduced with permission from Ref. [93], © American Chemical Society 2021.

binding ligands such as cadmium halide after the synthesis of 4 ML CdSe NPLs [88], as shown in Fig. 6(b). Considering the thermodynamics of monomers, the material transfer from thin NPLs to thicker NPLs during heating can be explained and tested [89, 90]. Due to the thermodynamic instability of thin NPLs compared to thicker NPLs, this transfer can occur even for thin NPLs with larger volumes, distinguishing it from the classical Ostwald ripening process.

The effects of chalcogenides on the thickness control are also demonstrated. The reaction intermediates generated in situ from the element sulfur or selenium are proposed to regulate supersaturation and the phase separation processes. Researchers demonstrate the formation of 3 MLs NPLs, 4 MLs NPLs, and QDs as a result of decreasing the reactivity of the bis(acyl) selenides by enhancing the electron-withdrawing ability of acyl groups, suggesting the reactivity-related supersaturation [91]. Reactive $(ODE\text{-}Se)_2$ is also found as an intermediate in the formation of NPLs, which is the product of the reduction of metallic Se by C=C double bonds of solvents.

The lateral morphology is of interest since it affects the optical properties as well as the colloidal properties [94–99], as shown in Fig. 6(d). Regarding size, the lateral morphology varies from around 5 nanometers to one hundred nanometers. Regarding shape, the lateral morphology exhibits shapes such as square, rectangle, and triangle [64, 92]. To quantitatively study the lateral morphology, researchers define the aspect ratio as the ratio of the length and width of rectangle NPLs.

Two lateral growth directions are identified as <100> and <110>, implying the asymmetry between lateral directions originates from the facet discrepancy [93]. The preference of <100> or <110> growth is tunable by introducing the hydroxide ions or the amount of added cadmium acetate. The hydroxide ions, generated by the decomposition of dihydrate cadmium acetate, are postulated to favor the growth along <100>. The impact of hydroxide ions is demonstrated by the utilization of cadmium hydroxide and anhydrous cadmium acetate, as shown in Fig. 6(e) [92]. Another regulation method is to simply increase the amount of added cadmium acetate, and then the dominant growth direction can be transformed from <100> to <110>. Further investigation reveals the wedge-shaped conformations along the <100> and <110> directions, that the exposed facets are {110} and {111} facets, respectively, not {100} and {110} facets as expected. According to first-principles calculations, the adsorption of cadmium acetate on {110} is then found to be energetically favorable under high Se coverage, while the {111} is favorable under low Se coverage, as shown in Fig. 6(f) [93].

With insights into morphology regulation, it is possible to fine-tune the vertical and lateral growth of NPLs, which lays the foundation for the heterostructure growth.

4.3 Heterostructures of NPLs

To improve the performance of NPLs, the growth of high bandgap materials around the NPLs is indispensable. According to the growth direction, the formed heterostructures have two types, the core/crown, unique in NPLs, and the core/shell, resembling QDs, heterostructure with the growth along the thickness direction is suppressed and permitted, respectively.

The core/crown heterostructure is realized by the lateral expansion of dissimilar materials, also called the core/wings heterostructure [100], as shown in Fig. 7(a). Due to the suppression growth along the vertical direction, the core/crown heterostructure can maintain the vertical quantum confinement in the core, as evidenced by the unaltered emission peaks during the crown growth. The crown can also be designed to increase the absorption in high-energy regions and enlarge the absorption cross-section.

The typical synthesis of a core/crown heterostructure involves two separate steps, the preparation of the core and the growth of the crown on the purified core. The crown growth shows an effective suppression of non-radiative processes thus increasing the PLQYs from 50% to 90% [101, 102]. This experimental observation is in line with the first-principles calculations, which suggest that surface traps are mainly located at the edge of NPLs [62].

Suppression of non-radiative processes can be further enhanced by the continuous synthesis of the crown, which forms the gradient composition that mitigates the interface defects [103]. This continuous synthesis grows the crown in situ during the core growth by introducing crown precursors, simplifying the synthesis procedure. The lateral size of the core can then be fixed by altering the timing of the crown precursor introduction, which provides a feasible way to control the lateral size of the cores, especially when small lateral size is required to mitigate the self-absorption effect and apply a lateral confinement effect, as shown in Fig. 7(b). Therefore, based on 4 and 5 ML CdSe NPLs, this method realizes the synthesis of CdSe/CdSeS core/crown heterostructures with near-unity PLQYs and emission tunability from 502 to 550 nm. The continuous crown growth method is also demonstrated to be effective in thinner 3 ML NPLs with emission peaking at 460 nm [64]. This research finds that the asymmetrical crown growth can achieve PLQYs of 90%, where the growth along the width direction is as thin as 0.9 nm, dramatically smaller than the 11.5 nm along the length direction. Furthermore, the lateral morphology is regulated by increasing the Cd-to-Se ratio, forming symmetrical core and crown growth, and achieving near-unity PLQYs. This result implies the necessity of a thick and symmetric heterostructure for the suppression of non-radiative processes in the core/crown structure.

Despite the high PLQYs of core/crown NPLs, the performance of LEDs based on these NPLs is unsatisfactory. The green and blue core/crown NPLs realize the NPL-LEDs with EQEs of 9.78% and 1.16%, respectively [63, 64]. However, the EQEs of these NPL-LEDs dramatically drops as the applied voltage increases, and the peak brightness of these NPL-LEDs can only achieve 2386 and 46 $cd \cdot m^{-2}$, respectively. These results may reflect the prominent deficiency of the crown, as the heterostructure is asymmetric when considering the vertical direction since there is no growth along that direction, in other words, the crown has no suppression effect along the vertical direction.

Therefore, the core/shell heterostructure that enables the vertical and lateral growth of dissimilar materials may provide insights. The methods to synthesize core/shell heterostructure can be categorized into two types, the colloidal atomic layer deposition (c-ALD) and the continuous methods. The c-ALD strategy distinguishes itself by the atomic precision of materials deposition [104]. The c-ALD strategy is to separate the deposition of metal and chalcogenides by the purification process, as shown in Fig. 7(c). By repeating the deposition and purification process, the thickness of the shell can be controlled at atomic preciseness and uniformity. In the preliminary stage, c-ALD is performed with phase transfer between polar and apolar solvents, which is complex and not feasible at elevated temperatures. The stationary phase c-ALD circumvents the requirement of the phase transfer by utilizing solid precursors, such as cadmium acetate and lithium sulfide [105]. This method enables the deposition of materials at an elevated temperature around 150 °C, and NPLs with PLQYs up to 91% and FWHMs down to 16.7 nm have been synthesized. Complex heterostructures are also obtained as shown in Fig. 7(d).

The continuous method allows the coexistence of metal and

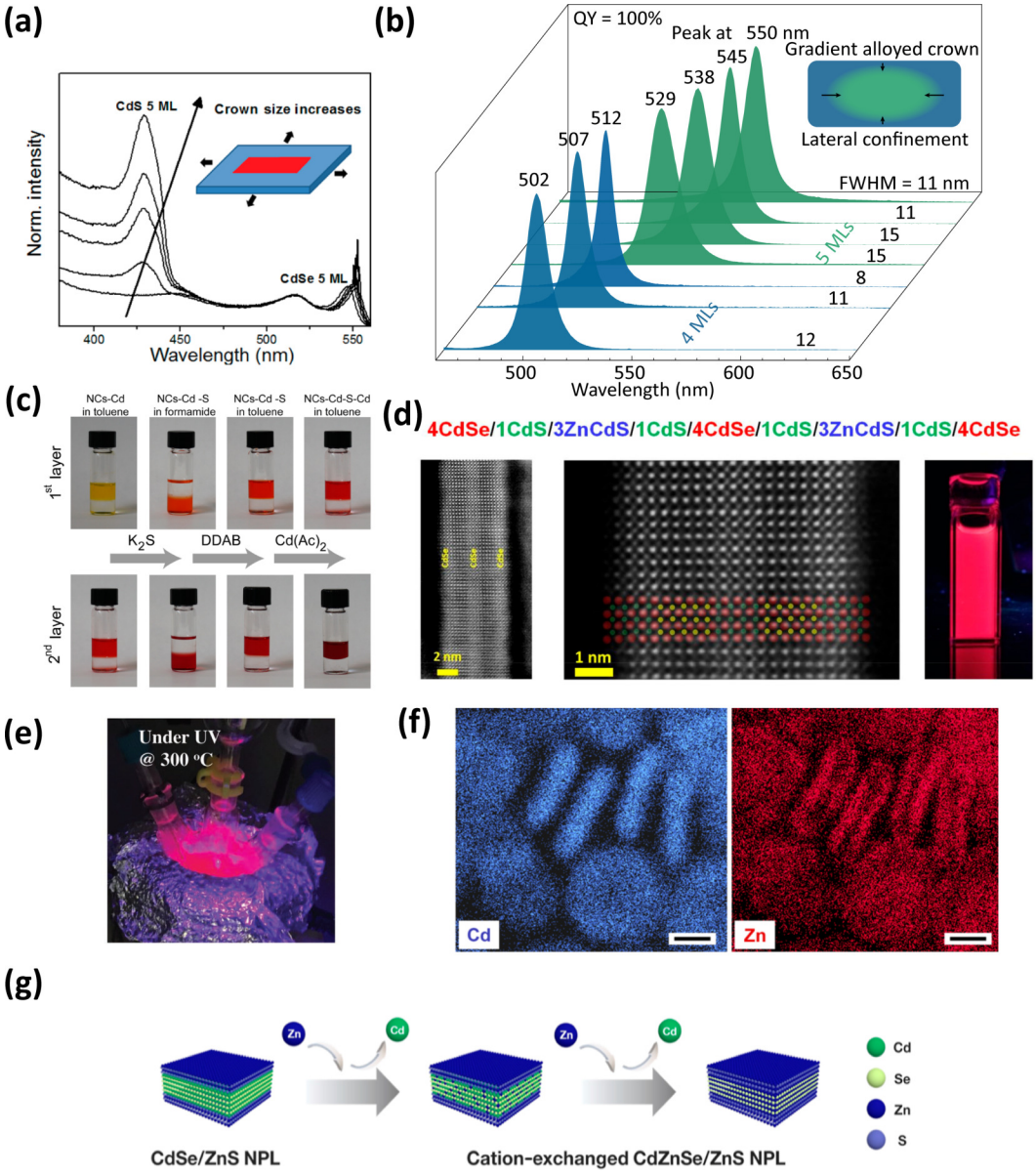

Figure 7 (a) Absorption spectra of CdSe/CdS core/crown NPLs with different crown sizes. Reproduced with permission from Ref. [100], © American Chemical Society 2013. (b) Emission spectra of CdSe/CdSeS core/crown NPLs with different core sizes. Reproduced with permission from Ref. [103], © Wiley-VCH GmbH 2022. (c) Photographs of sequential growth of two layers of CdS shell on CdSe NPLs. Reproduced with permission from Ref. [104], © American Chemical Society 2012. (d) Atomically resolved electron microscopy images of complex NPL heterostructures. Reproduced with permission from Ref. [105], © American Chemical Society 2019. (e) Photographs of excited core/shell NPLs at 300 °C using the continuous shell method. Reproduced with permission from Ref. [106], © WILEY-VCH Verlag GmbH ~ Co. KGaA, Weinheim 2019. (f) The element analysis of CdSe/ZnS core/shell NPLs. The scale bars are 5 nm. Reproduced with permission from Ref. [107], © American Chemical Society 2019. (g) Illustration of Cd-to-Zn cation exchange reaction of CdSe/ZnS NPLs. Reproduced with permission from Ref. [108], © American Chemical Society 2022.

chalcogenide precursors during the shell growth [33, 71], and thus the process is much simplified compared to c-ALD. Due to the outstanding optical performance of the synthesized NPLs, the continuous method performed at elevated reaction temperatures has attracted popularity [106, 109]. At elevated temperatures near 300 °C, the dissolution of NPLs becomes inevitable, and to stabilize NPLs, researchers have devised methods such as the addition of metal salts and chalcogenide precursors at a low temperature, resulting in NPLs with near unity PLQYs and high thermal stability, as shown in Fig. 7(e). This method also permits the compositional gradient that reduces crystal defects [107], emission FWHMs, and Auger rate [73], as shown in Fig. 7(f).

The applicability of the continuous method, however, is limited by the core thickness requirement, that NPLs with a thin thickness will soon dissolve under an elevated temperature. This limitation leads to a poor emission tunability of core/shell NPLs, with emission peaking at yellow to red regions. The cation exchange method provides another approach to forming a shell not by growing dissimilar materials but by replacing the original materials [108, 110], as shown in Fig. 7(g). This method can tune the composition of the core by doping sulfur or controlling the Cd-to-Zn cation exchange using ZnI_2 and oleylamine, providing a wide range of emission tunability reaching 425 nm.

5 Progress of assembling NPLs in devices

The dipole of a single NPL is in-plane, but the overall dipole of multiple NPLs will be random when assembly is uncontrolled. When all dipoles are aligned horizontally, the efficiency of devices can be improved. Therefore, the assembly of NPLs with a "face-down" configuration in devices is preferred. The pure "face-down" configuration can be realized by the liquid interfacial self-assembly which controls the assembly of CdSe NPLs at the interface of top

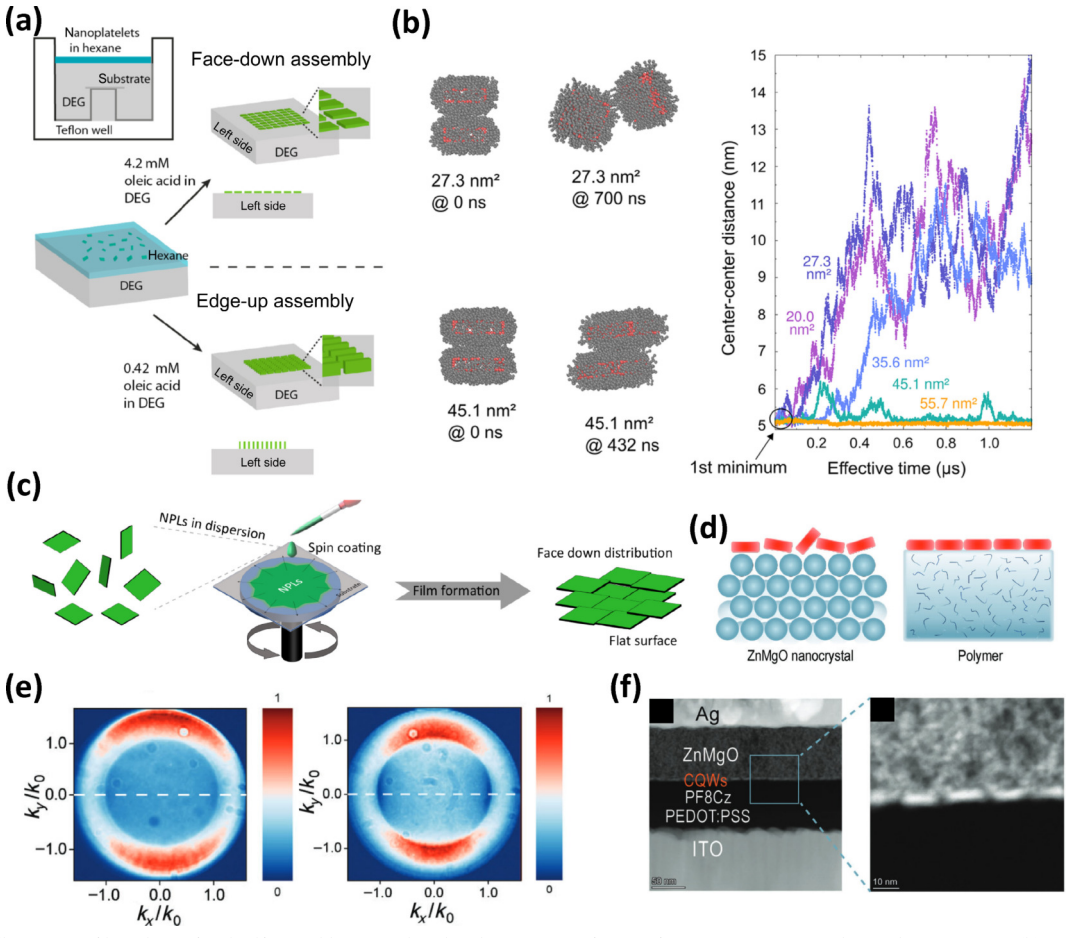

Figure 8 (a) Illustration of liquid interfacial self-assembly. Reproduced with permission from Ref. [111], © American Chemical Society 2017. (b) Snapshots of stack dynamics and a center-center distances evolution of NPLs with different facet areas, obtained by unconstrained molecular simulations. Reproduced with permission from Ref. [115], © Petersen, N. et al. 2022. (c) Illustration of spin-coating self-assembly. Reproduced with permission from Ref. [63], © American Chemical Society 2022. (d) Illustration of the arrangement of NPLs on different substrates, (e) experimental back focus plane images of films prepared from solution with NPL concentrations of 64 (left) and 8 (right) mg·mL^{-1}, and (f) the cross-sectional high-angle annular dark-field scanning transmission electron microscopy (HAADF-STEM) image of NPL-LEDs. Reproduced with permission from Ref. [34], © Wiley-VCH GmbH 2023.

and down phases, which utilize the van der Waals interactions between the ligands and the liquid molecules [111]. The amount of oleic acid added is discovered to control the assembly of NPLs being "face-down" or "edge-up", as shown in Fig. 8(a). Recent research suggests that the evaporation kinetics of the top phase also determines the assembly behavior, that fast evaporation leads to a "face-down" configuration and slow evaporation leads to an "edge-up" configuration [112].

The use of polar solvents, such as acetonitrile, in the liquid interface self-assembly is not suitable when polar solvents can dissolve the substrate [112, 113], i.e., the ZnO layer in the LED fabrication. Therefore, drop-wise assembly methods that form a smooth film have gained interest, and where the interaction between NPLs and molecules and other NPLs in the polar solvents is essential [114]. To achieve a "face-down" configuration, one must suppress the stacking effect that is prominent in the "edge-up" configuration. According to coarse-grained molecular dynamics simulations, the strong solvation forces give rise to the strong stacking effect in NPLs, and the solvation forces are proportional to the facet area and can be weakened by softening the ligands [115], as shown in Fig. 8(b). The simulation results are consistent with a series of research which have concluded that, besides the evaporation kinetics, the lateral morphology [63], the ligands [63], the NPL concentration [34], and the configuration of the substrate [34] are vital to the assemble controllability. As shown in Fig. 8(c), spin-coating assembly is achieved via the regulation on lateral morphology and ligands. The smooth substrate is also proven to be vital for the "face-down" configuration, as shown in Figs. 8(d) and 8(e). With these advances, CdSe/CdZnS core/shell NPL LEDs with a single layer "face-down" configuration, as shown in Fig. 8(f), are achieved, exhibiting external quantum efficiencies (EQEs) up to 26.9%, which surpasses the theoretical maximum of 20% based on QDs [34].

6 Perspectives of NPLs for devices

NPLs have shown advantages in devices and an immense potential to be harvested. We have demonstrated that symmetrical shell growth is critical for the performance of NPLs and NPL devices. However, the symmetrical shell growth conflicts with the asymmetrical morphology of NPLs, which is thermodynamically stable. To reconcile this conflict during the shell growth, researchers have used highly reactive precursors, in the case of the c-ALD method, or elevated temperatures, in the case of the continuous growth method to realize high-performance NPLs and NPL devices. However, highly reactive precursors dramatically complicate the process and elevated temperatures degrade uniformity. While progress has been made in simplifying the c-ALD process and maintaining uniformity in the continuous method [105, 107], the performance of zinc-based NPLs and blue and green NPL LEDs remain inferior.

NPLs and QDs based on elements that are abundant and environmentally friendly have garnered attentions, due to the exceptional toxicity of Cd, which raises many concerns regarding

research safety and commercial usage. Zn is a promising candidate to address the environmental challenge. On the one hand, Zn could replace Cd via the cation exchange, lowering the concentration of Cd in the final products [116, 117]. On the other hand, incorporating zinc chalcogenides as core materials or as shell materials around indium phosphide could evade the usage of Cd [118, 119]. For instance, ZnSe or ZnTe with bandgaps of 2.70 and 2.25 eV, respectively, could provide a broad emission tunability in the visible light range, making them suitable candidate as the core materials.

However, the morphology regulation of these Zn-based NPLs is still at an early stage, and Zn-based NPLs with emission in the visible light region or with heterostructures have rarely been reported, not to mention the devices fabricated with these zinc-based NPLs. There are reports on the synthesis of ZnS [120−122], ZnSe [80, 84, 123], and ZnTe [124] wurtzite NPLs. These reported wurtzite ZnSe NPLs, for instance, show high aspect ratio and large lateral area. The thickness of these NPLs is around 1.4 nm and is expected to be fixed due to the high formation energy of an additional layer [85]. This result suggests that a reaction temperature of 760 K is required to overcome the energy barrier. However, the high temperature could convert the NPLs into other species such as quantum dots and nanowires. Fortunately, it seems that utilizing precursors with high reactivity could facilitate the growth of ZnS shell around these ZnSe wurtzite NPLs [125]. This may imply that ligands that can maintain the NPL morphology and reactive precursors that can lower the formation barrier may be worth developing to enhance the morphology controllability of wurtzite NPLs.

The synthesis of zinc-blende ZnSe NPLs can be classified by the indirect and direct synthesis. It is found that 1.4 nm wurtzite ZnSe NPLs could be transformed into 1.84 nm zinc-blende ZnSe NPLs by overdosing the Se precursor *in situ*, exhibiting emission centered at 380 nm and FWHM of 4.4 nm [80]. Interestingly, these NPLs show that {110} facet is the wide facet, unlike the typical zinc-blende CdSe NPLs, but further extending the thickness has not been reported. Besides the overdosing of precursor, Mn-assisted phase transfer can also realize the transform of wurtzite ZnSe NPLs to zinc-blende ZnSe NPLs [126]. And, Zinc-blende ZnSe NPLs could also be synthesized by the cation exchange [127]. Only recently has the direct synthesis of zinc-blende ZnSe NPLs been realized by utilizing zinc acetate and zinc chloride [128]. The synthesized NPLs also shows {110} facet is the wide facet and possess a maximum thickness of 1.46 nm. Therefore, the underlying mechanisms that can guide the vertical and lateral growth of these zinc-based NPLs need further discovery.

Additionally, blue and green NPL-LEDs with EQEs above 20% have remained unachieved. In these two regions, NPLs usually have a core/crown heterostructure that cannot provide sufficient spatial and potential separation between exciton and surface traps, especially along the vertical direction. This inability of core/crown heterostructures leads to inferior device performance. As discussed, the symmetric shell is critical to the device performance, but can also redshift emissions by relaxing the vertical confinement. Therefore, Cd-to-Zn exchanged NPLs or the Zn-based NPLs may be suitable for achieving high-performance blue and green NPL LEDs. Further exploration of growth control will improve the performance of NPL-LEDs and potentially realize Auger minima, which could dramatically decrease the lasing threshold. Along with investigations on the electrochemistry [129, 130] and exciton dynamics in novel heterostructures [20, 131], we expect a deepened understanding of the relationships between NPL structure and device performance, which could allow the lasing threshold to be further decreased [132]. Finally, we anticipate the development of high-performance NPL devices with desired properties. Toward this broader objective, numerous exciting mysteries await resolution.

Acknowledgements

This project is supported by the National Natural Science Foundation of China (Nos. 62375004 and 61875002), China Postdoctoral Science Foundation (Nos. 2023M731476, 2023T160286 and 2024M751274), and Beijing Postdoctoral Research Foundation.

References

[1] Joo, J.; Son, J. S.; Kwon, S. G.; Yu, J. H.; Hyeon, T. Low-temperature solution-phase synthesis of quantum well structured CdSe nanoribbons. *J. Am. Chem. Soc.* **2006**, *128*, 5632–5633.

[2] Ithurria, S.; Dubertret, B. Quasi 2D colloidal CdSe platelets with thicknesses controlled at the atomic level. *J. Am. Chem. Soc.* **2008**, *130*, 16504–16505.

[3] Ithurria, S.; Tessier, M. D.; Mahler, B.; Lobo, R. P. S. M.; Dubertret, B.; Efros, A. L. Colloidal nanoplatelets with two-dimensional electronic structure. *Nat. Mater.* **2011**, *10*, 936–941.

[4] Sanderson, K.; Castelvecchi, D. Tiny "Quantum Dot" particles win chemistry Nobel. *Nature* **2023**, *622*, 227–228.

[5] Arakawa, Y.; Sakaki, H. Multidimensional quantum well laser and temperature dependence of its threshold current. *Appl. Phys. Lett.* **1982**, *40*, 939–941.

[6] Zhou, J. H.; Zhu, M. Y.; Meng, R. Y.; Qin, H. Y.; Peng, X. G. Ideal CdSe/CdS core/shell nanocrystals enabled by entropic ligands and their core size-, shell thickness-, and ligand-dependent photoluminescence properties. *J. Am. Chem. Soc.* **2017**, *139*, 16556–16567.

[7] Huang, L.; Ye, Z. K.; Yang, L.; Li, J. Z.; Qin, H. Y.; Peng, X. G. Synthesis of colloidal quantum dots with an ultranarrow photoluminescence peak. *Chem. Mater.* **2021**, *33*, 1799–1810.

[8] Dai, X. L.; Zhang, Z. X.; Jin, Y. Z.; Niu, Y.; Cao, H. J.; Liang, X. Y.; Chen, L. W.; Wang, J. P.; Peng, X. G. Solution-processed, high-performance light-emitting diodes based on quantum dots. *Nature* **2014**, *515*, 96–99.

[9] Ahn, N.; Livache, C.; Pinchetti, V.; Jung, H.; Jin, H.; Hahm, D.; Park, Y. S.; Klimov, V. I. Electrically driven amplified spontaneous emission from colloidal quantum dots. *Nature* **2023**, *617*, 79–85.

[10] Chen, D. D.; Gao, Y.; Chen, Y. Y.; Ren, Y.; Peng, X. G. Structure identification of two-dimensional colloidal semiconductor nanocrystals with atomic flat basal planes. *Nano Lett.* **2015**, *15*, 4477–4482.

[11] Zhang, J.; Sun, Y.; Ye, S.; Song, J.; Qu, J. L. Heterostructures in two-dimensional CdSe nanoplatelets: Synthesis, optical properties, and applications. *Chem. Mater.* **2020**, *32*, 9490–9507.

[12] Pun, A. B.; Mazzotti, S.; Mule, A. S.; Norris, D. J. Understanding discrete growth in semiconductor nanocrystals: Nanoplatelets and magic-sized clusters. *Acc. Chem. Res.* **2021**, *54*, 1545–1554.

[13] Bai, B.; Zhang, C. X.; Dou, Y. J.; Kong, L. M.; Wang, L.; Wang, S.; Li, J.; Zhou, Y.; Liu, L.; Liu, B. Q. et al. Atomically flat semiconductor nanoplatelets for light-emitting applications. *Chem. Soc. Rev.* **2023**, *52*, 318–360.

[14] Diroll, B. T.; Guzelturk, B.; Po, H.; Dabard, C.; Fu, N. Y.; Makke, L.; Lhuillier, E.; Ithurria, S. 2D II-VI semiconductor nanoplatelets: From material synthesis to optoelectronic integration. *Chem. Rev.* **2023**, *123*, 3543–3624.

[15] Vaxenburg, R.; Rodina, A.; Shabaev, A.; Lifshitz, E.; Efros, A. L. Nonradiative auger recombination in semiconductor nanocrystals. *Nano Lett.* **2015**, *15*, 2092–2098.

[16] Pelton, M.; Andrews, J. J.; Fedin, I.; Talapin, D. V.; Leng, H. X.; O' Leary, S. K. Nonmonotonic dependence of auger recombination rate on shell thickness for CdSe/CdS core/shell nanoplatelets. *Nano Lett.* **2017**, *17*, 6900–6906.

[17] Philbin, J. P.; Brumberg, A.; Diroll, B. T.; Cho, W.; Talapin, D. V.;

Schaller, R. D.; Rabani, E. Area and thickness dependence of auger recombination in nanoplatelets. *J. Chem. Phys.* **2020**, *153*, 054104.

[18] Li, Q. Y.; Lian, T. Q. Area- and thickness-dependent biexciton auger recombination in colloidal CdSe nanoplatelets: Breaking the "universal volume scaling law". *Nano Lett.* **2017**, *17*, 3152–3158.

[19] She, C. X.; Fedin, I.; Dolzhnikov, D. S.; Dahlberg, P. D.; Engel, G. S.; Schaller, R. D.; Talapin, D. V. Red, yellow, green, and blue amplified spontaneous emission and lasing using colloidal CdSe nanoplatelets. *ACS Nano* **2015**, *9*, 9475–9485.

[20] Taghipour, N.; Delikanli, S.; Shendre, S.; Sak, M.; Li, M. J.; Isik, F.; Tanriover, I.; Guzelturk, B.; Sum, T. C.; Demir, H. V. Sub-single exciton optical gain threshold in colloidal semiconductor quantum wells with gradient alloy shelling. *Nat. Commun.* **2020**, *11*, 3305.

[21] Geiregat, P.; Rodá, C.; Tanghe, I.; Singh, S.; Di Giacomo, A.; Lebrun, D.; Grimaldi, G.; Maes, J.; Van Thourhout, D.; Moreels, I. et al. Localization-limited exciton oscillator strength in colloidal CdSe nanoplatelets revealed by the optically induced stark effect. *Light: Sci. Appl.* **2021**, *10*, 112.

[22] Hens, Z.; Moreels, I. Light absorption by colloidal semiconductor quantum dots. *J. Mater. Chem.* **2012**, *22*, 10406–10415.

[23] Sharma, M.; Gungor, K.; Yeltik, A.; Olutas, M.; Guzelturk, B.; Kelestemur, Y.; Erdem, T.; Delikanli, S.; McBride, J. R.; Demir, H. V. Near-unity emitting copper-doped colloidal semiconductor quantum wells for luminescent solar concentrators. *Adv. Mater.* **2017**, *29*, 1700821.

[24] Park, Y. S.; Lim, J.; Klimov, V. I. Asymmetrically strained quantum dots with non-fluctuating single-dot emission spectra and subthermal room-temperature linewidths. *Nat. Mater.* **2019**, *18*, 249–255.

[25] Erdem, T.; Soran-Erdem, Z.; Isik, F.; Shabani, F.; Yazici, A. F.; Mutlugün, E.; Gaponik, N.; Demir, H. V. Color enrichment solids of spectrally pure colloidal quantum wells for wide color span in displays. *Adv. Opt. Mater.* **2022**, *10*, 2200161.

[26] Jung, H.; Ahn, N.; Klimov, V. I. Prospects and challenges of colloidal quantum dot laser diodes. *Nat. Photonics* **2021**, *15*, 643–655.

[27] Ma, X. D.; Diroll, B. T.; Cho, W.; Fedin, I.; Schaller, R. D.; Talapin, D. V.; Wiederrecht, G. P. Anisotropic photoluminescence from isotropic optical transition dipoles in semiconductor nanoplatelets. *Nano Lett.* **2018**, *18*, 4647–4652.

[28] Achtstein, A. W.; Schliwa, A.; Prudnikau, A.; Hardzei, M.; Artemyev, M. V.; Thomsen, C.; Woggon, U. Electronic structure and exciton-phonon interaction in two-dimensional colloidal CdSe nanosheets. *Nano Lett.* **2012**, *12*, 3151–3157.

[29] Scott, R.; Heckmann, J.; Prudnikau, A. V.; Antanovich, A.; Mikhailov, A.; Owschimikow, N.; Artemyev, M.; Climente, J. I.; Woggon, U.; Grosse, N. B. et al. Directed emission of CdSe nanoplatelets originating from strongly anisotropic 2D electronic structure. *Nat. Nanotechnol.* **2017**, *12*, 1155–1160.

[30] Yoon, D. E.; Kim, W. D.; Kim, D.; Lee, D.; Koh, S.; Bae, W. K.; Lee, D. C. Origin of shape-dependent fluorescence polarization from CdSe nanoplatelets. *J. Phys. Chem. C* **2017**, *121*, 24837–24844.

[31] Cunningham, P. D.; Souza, J. B.; Fedin, I.; She, C. X.; Lee, B.; Talapin, D. V. Assessment of anisotropic semiconductor nanorod and nanoplatelet heterostructures with polarized emission for liquid crystal display technology. *ACS Nano* **2016**, *10*, 5769–5781.

[32] Fan, F. J.; Voznyy, O.; Sabatini, R. P.; Bicanic, K. T.; Adachi, M. M.; McBride, J. R.; Reid, K. R.; Park, Y. S.; Li, X. Y.; Jain, A. et al. Continuous-wave lasing in colloidal quantum dot solids enabled by facet-selective epitaxy. *Nature* **2017**, *544*, 75–79.

[33] Tessier, M. D.; Mahler, B.; Nadal, B.; Heuclin, H.; Pedetti, S.; Dubertret, B. Spectroscopy of colloidal semiconductor core/shell nanoplatelets with high quantum yield. *Nano Lett.* **2013**, *13*, 3321–3328.

[34] Zhu, Y. K.; Deng, Y. Z.; Bai, P.; Wu, X. N.; Yao, Y. G.; Liu, Q. Y.; Qiu, J. J.; Hu, A.; Tang, Z. Y.; Yu, W. J. et al. Highly efficient light-emitting diodes based on self-assembled colloidal quantum wells. *Adv. Mater.* **2023**, *35*, 2305382.

[35] Califano, M.; Gómez-Campos, F. M. Universal trapping mechanism in semiconductor nanocrystals. *Nano Lett.* **2013**, *13*, 2047–2052.

[36] Rowland, C. E.; Fedin, I.; Zhang, H.; Gray, S. K.; Govorov, A. O.; Talapin, D. V.; Schaller, R. D. Picosecond energy transfer and multiexciton transfer outpaces auger recombination in binary CdSe nanoplatelet solids. *Nat. Mater.* **2015**, *14*, 484–489.

[37] Guzelturk, B.; Erdem, O.; Olutas, M.; Kelestemur, Y.; Demir, H. V. Stacking in colloidal nanoplatelets: Tuning excitonic properties. *ACS Nano* **2014**, *8*, 12524–12533.

[38] Chen, O.; Zhao, J.; Chauhan, V. P.; Cui, J.; Wong, C.; Harris, D. K.; Wei, H.; Han, H. S.; Fukumura, D.; Jain, R. K. et al. Compact high-quality CdSe–CdS core–shell nanocrystals with narrow emission linewidths and suppressed blinking. *Nat. Mater.* **2013**, *12*, 445–451.

[39] Hou, X. Q.; Kang, J.; Qin, H. Y.; Chen, X. W.; Ma, J. L.; Zhou, J. H.; Chen, L. P.; Wang, L. J.; Wang, L. W.; Peng, X. G. Engineering auger recombination in colloidal quantum dots via dielectric screening. *Nat. Commun.* **2019**, *10*, 1750.

[40] García-Santamaría, F.; Brovelli, S.; Viswanatha, R.; Hollingsworth, J. A.; Htoon, H.; Crooker, S. A.; Klimov, V. I. Breakdown of volume scaling in auger recombination in CdSe/CdS heteronanocrystals: The role of the core–shell interface. *Nano Lett.* **2011**, *11*, 687–693.

[41] Bae, W. K.; Padilha, L. A.; Park, Y. S.; McDaniel, H.; Robel, I.; Pietryga, J. M.; Klimov, V. I. Controlled alloying of the core–shell interface in CdSe/CdS quantum dots for suppression of auger recombination. *ACS Nano* **2013**, *7*, 3411–3419.

[42] Endres, E. J.; Bairan Espano, J. R.; Koziel, A.; Peng, A. R.; Shults, A. A.; Macdonald, J. E. Controlling phase in colloidal synthesis. *ACS Nanosci. Au* **2024**, *4*, 158–175.

[43] Kim, T.; Kim, K. H.; Kim, S.; Choi, S. M.; Jang, H.; Seo, H. K.; Lee, H.; Chung, D. Y.; Jang, E. Efficient and stable blue quantum dot light-emitting diode. *Nature* **2020**, *586*, 385–389.

[44] Ghosh, Y.; Mangum, B. D.; Casson, J. L.; Williams, D. J.; Htoon, H.; Hollingsworth, J. A. New insights into the complexities of shell growth and the strong influence of particle volume in nonblinking "Giant" core/shell nanocrystal quantum dots. *J. Am. Chem. Soc.* **2012**, *134*, 9634–9643.

[45] Galland, C.; Ghosh, Y.; Steinbrück, A.; Hollingsworth, J. A.; Htoon, H.; Klimov, V. I. Lifetime blinking in nonblinking nanocrystal quantum dots. *Nat. Commun.* **2012**, *3*, 908.

[46] Bradshaw, L. R.; Knowles, K. E.; McDowall, S.; Gamelin, D. R. Nanocrystals for luminescent solar concentrators. *Nano Lett.* **2015**, *15*, 1315–1323.

[47] Lorenzon, M.; Christodoulou, S.; Vaccaro, G.; Pedrini, J.; Meinardi, F.; Moreels, I.; Brovelli, S. Reversed oxygen sensing using colloidal quantum wells towards highly emissive photoresponsive varnishes. *Nat. Commun.* **2015**, *6*, 6434.

[48] Larson, D. R.; Zipfel, W. R.; Williams, R. M.; Clark, S. W.; Bruchez, M. P.; Wise, F. W.; Webb, W. W. Water-soluble quantum dots for multiphoton fluorescence imaging *in vivo*. *Science* **2003**, *300*, 1434–1436.

[49] Lim, J.; Park, Y. S.; Klimov, V. I. Optical gain in colloidal quantum dots achieved with direct-current electrical pumping. *Nat. Mater.* **2018**, *17*, 42–49.

[50] Lim, J.; Park, Y. S.; Wu, K. F.; Yun, H. J.; Klimov, V. I. Droop-free colloidal quantum dot light-emitting diodes. *Nano Lett.* **2018**, *18*, 6645–6653.

[51] Lee, T.; Kim, B. J.; Lee, H.; Hahm, D.; Bae, W. K.; Lim, J.; Kwak, J. Bright and stable quantum dot light-emitting diodes. *Adv. Mater.* **2022**, *34*, 2106276.

[52] Ahn, N.; Livache, C.; Pinchetti, V.; Klimov, V. I. Colloidal semiconductor nanocrystal lasers and laser diodes. *Chem. Rev.* **2023**, *123*, 8251–8296.

[53] Cragg, G. E.; Efros, A. L. Suppression of auger processes in confined structures. *Nano Lett.* **2010**, *10*, 313–317.

[54] Climente, J. I.; Movilla, J. L.; Planelles, J. Auger recombination suppression in nanocrystals with asymmetric electron–hole confinement. *Small* **2012**, *8*, 754–759.

[55] Deng, Y. Z.; Peng, F.; Lu, Y.; Zhu, X. T.; Jin, W. X.; Qiu, J.; Dong, J. W.; Hao, Y. L.; Di, D. W.; Gao, Y. et al. Solution-processed

green and blue quantum-dot light-emitting diodes with eliminated charge leakage. *Nat. Photonics* **2022**, *16*, 505–511.
[56] Kim, W. D.; Kim, D.; Yoon, D. E.; Lee, H.; Lim, J.; Bae, W. K.; Lee, D. C. Pushing the efficiency envelope for semiconductor nanocrystal-based electroluminescence devices using anisotropic nanocrystals. *Chem. Mater.* **2019**, *31*, 3066–3082.
[57] Jang, E.; Jang, H. Review: Quantum dot light-emitting diodes. *Chem. Rev.* **2023**, *123*, 4663–4692.
[58] Kim, J.; Roh, J.; Park, M.; Lee, C. Recent advances and challenges of colloidal quantum dot light-emitting diodes for display applications. *Adv. Mater.* **2024**, *36*, 2212220.
[59] Vashchenko, A. A.; Vitukhnovskii, A. G.; Lebedev, V. S.; Selyukov, A. S.; Vasiliev, R. B.; Sokolikova, M. S. Organic light-emitting diode with an emitter based on a planar layer of CdSe semiconductor nanoplatelets. *JETP Lett.* **2014**, *100*, 86–90.
[60] Liu, J. W.; Guillemeney, L.; Abécassis, B.; Coolen, L. Long range energy transfer in self-assembled stacks of semiconducting nanoplatelets. *Nano Lett.* **2020**, *20*, 3465–3470.
[61] Guzelturk, B.; Olutas, M.; Delikanli, S.; Kelestemur, Y.; Erdem, O.; Demir, H. V. Nonradiative energy transfer in colloidal CdSe nanoplatelet films. *Nanoscale* **2015**, *7*, 2545–2551.
[62] Singh, S.; Tomar, R.; Ten Brinck, S.; De Roo, J.; Geiregat, P.; Martins, J. C.; Infante, I.; Hens, Z. Colloidal CdSe nanoplatelets, a model for surface chemistry/optoelectronic property relations in semiconductor nanocrystals. *J. Am. Chem. Soc.* **2018**, *140*, 13292–13300.
[63] Bai, P.; Hu, A.; Deng, Y. Z.; Tang, Z. Y.; Yu, W. J.; Hao, Y. L.; Yang, S.; Zhu, Y. K.; Xiao, L. X.; Jin, Y. Z. et al. CdSe/CdSeS nanoplatelet light-emitting diodes with ultrapure green color and high external quantum efficiency. *J. Phys. Chem. Lett.* **2022**, *13*, 9051–9057.
[64] Hu, A.; Bai, P.; Zhu, Y. K.; Tang, Z. Y.; Xiao, L. X.; Gao, Y. M. Controlled core/crown growth enables blue-emitting colloidal nanoplatelets with efficient and pure photoluminescence. *Small* **2022**, *18*, 2204120.
[65] Fan, F. J.; Kanjanaboos, P.; Saravanapavanantham, M.; Beauregard, E.; Ingram, G.; Yassitepe, E.; Adachi, M. M.; Voznyy, O.; Johnston, A. K.; Walters, G. et al. Colloidal $CdSe_{1-x}S_x$ nanoplatelets with narrow and continuously-tunable electroluminescence. *Nano Lett.* **2015**, *15*, 4611–4615.
[66] Zhang, F. J.; Wang, S. J.; Wang, L.; Lin, Q. L.; Shen, H. B.; Cao, W. R.; Yang, C. C.; Wang, H. Z.; Yu, L.; Du, Z. L. et al. Super color purity green quantum dot light-emitting diodes fabricated by using CdSe/CdS nanoplatelets. *Nanoscale* **2016**, *8*, 12182–12188.
[67] Liu, B. Q.; Sharma, M.; Yu, J. H.; Shendre, S.; Hettiarachchi, C.; Sharma, A.; Yeltik, A.; Wang, L.; Sun, H. D.; Dang, C. N. et al. Light-emitting diodes with Cu-doped colloidal quantum wells: From ultrapure green, tunable dual-emission to white light. *Small* **2019**, *15*, 1901983.
[68] Chen, Z. Y.; Nadal, B.; Mahler, B.; Aubin, H.; Dubertret, B. Quasi-2D colloidal semiconductor nanoplatelets for narrow electroluminescence. *Adv. Funct. Mater.* **2014**, *24*, 295–302.
[69] Giovanella, U.; Pasini, M.; Lorenzon, M.; Galeotti, F.; Lucchi, C.; Meinardi, F.; Luzzati, S.; Dubertret, B.; Brovelli, S. Efficient solution-processed nanoplatelet-based light-emitting diodes with high operational stability in air. *Nano Lett.* **2018**, *18*, 3441–3448.
[70] Kelestemur, Y.; Shynkarenko, Y.; Anni, M.; Yakunin, S.; De Giorgi, M. L.; Kovalenko, M. V. Colloidal CdSe quantum wells with graded shell composition for low-threshold amplified spontaneous emission and highly efficient electroluminescence. *ACS Nano* **2019**, *13*, 13899–13909.
[71] Liu, B. Q.; Altintas, Y.; Wang, L.; Shendre, S.; Sharma, M.; Sun, H. D.; Mutlugun, E.; Demir, H. V. Record high external quantum efficiency of 19.2% achieved in light-emitting diodes of colloidal quantum wells enabled by hot-injection shell growth. *Adv. Mater.* **2020**, *32*, 1905824.
[72] Qu, J. L.; Rastogi, P.; Gréboval, C.; Livache, C.; Dufour, M.; Chu, A.; Chee, S. S.; Ramade, J.; Xu, X. Z.; Ithurria, S. et al. Nanoplatelet-based light-emitting diode and its use in all-nanocrystal LiFi-like communication. *ACS Appl. Mater. Interfaces* **2020**, *12*, 22058–22065.
[73] Liang, X.; Durmusoglu, E. G.; Lunina, M.; Hernandez-Martinez, P. L.; Valuckas, V.; Yan, F.; Lekina, Y.; Sharma, V. K.; Yin, T. T.; Ha, S. T. et al. Near-unity emitting, widely tailorable, and stable exciton concentrators built from doubly gradient 2D semiconductor nanoplatelets. *ACS Nano* **2023**, *17*, 19981–19992.
[74] Son, J. S.; Wen, X. D.; Joo, J.; Chae, J.; Baek, S. I.; Park, K.; Kim, J. H.; An, K.; Yu, J. H.; Kwon, S. G. et al. Large-scale soft colloidal template synthesis of 1.4 Nm thick CdSe nanosheets. *Angew. Chem., Int. Ed.* **2009**, *48*, 6861–6864.
[75] Son, J. S.; Park, K.; Kwon, S. G.; Yang, J.; Choi, M. K.; Kim, J.; Yu, J. H.; Joo, J.; Hyeon, T. Dimension-controlled synthesis of CdS nanocrystals: From 0D quantum dots to 2D nanoplates. *Small* **2012**, *8*, 2394–2402.
[76] Morrison, P. J.; Loomis, R. A.; Buhro, W. E. Synthesis and growth mechanism of lead sulfide quantum platelets in lamellar mesophase templates. *Chem. Mater.* **2014**, *26*, 5012–5019.
[77] Wang, Y. Y.; Zhang, Y.; Wang, F. D.; Giblin, D. E.; Hoy, J.; Rohrs, H. W.; Loomis, R. A.; Buhro, W. E. The magic-size nanocluster $(CdSe)_{34}$ as a low-temperature nucleant for cadmium selenide nanocrystals; room-temperature growth of crystalline quantum platelets. *Chem. Mater.* **2014**, *26*, 2233–2243.
[78] Wang, Y. Y.; Zhou, Y.; Zhang, Y.; Buhro, W. E. Magic-size II-VI nanoclusters as synthons for flat colloidal nanocrystals. *Inorg. Chem.* **2015**, *54*, 1165–1177.
[79] Nasilowski, M.; Mahler, B.; Lhuillier, E.; Ithurria, S.; Dubertret, B. Two-dimensional colloidal nanocrystals. *Chem. Rev.* **2016**, *116*, 10934–10982.
[80] Cunningham, P. D.; Coropceanu, I.; Mulloy, K.; Cho, W.; Talapin, D. V. Quantized reaction pathways for solution synthesis of colloidal ZnSe nanostructures: A connection between clusters, nanowires, and two-dimensional nanoplatelets. *ACS Nano* **2020**, *14*, 3847–3857.
[81] Riedinger, A.; Ott, F. D.; Mule, A.; Mazzotti, S.; Knüsel, P. N.; Kress, S. J. P.; Prins, F.; Erwin, S. C.; Norris, D. J. An intrinsic growth instability in isotropic materials leads to quasi-two-dimensional nanoplatelets. *Nat. Mater.* **2017**, *16*, 743–748.
[82] Li, Z.; Peng, X. G. Size/shape-controlled synthesis of colloidal CdSe quantum disks: Ligand and temperature effects. *J. Am. Chem. Soc.* **2011**, *133*, 6578–6586.
[83] Gerdes, F.; Navío, C.; Juárez, B. H.; Klinke, C. Size, shape, and phase control in ultrathin CdSe nanosheets. *Nano Lett.* **2017**, *17*, 4165–4171.
[84] Park, H.; Chung, H.; Kim, W. Synthesis of ultrathin wurtzite ZnSe nanosheets. *Mater. Lett.* **2013**, *99*, 172–175.
[85] Pang, Y. P.; Zhang, M. Y.; Chen, D. C.; Chen, W.; Wang, F.; Anwar, S. J.; Saunders, M.; Rowles, M. R.; Liu, L. H.; Liu, S. M. et al. Why do colloidal wurtzite semiconductor nanoplatelets have an atomically uniform thickness of eight monolayers. *J. Phys. Chem. Lett.* **2019**, *10*, 3465–3471.
[86] Sun, H. C.; Wang, F. D.; Buhro, W. E. Tellurium precursor for nanocrystal synthesis: Tris(dimethylamino)phosphine telluride. *ACS Nano* **2018**, *12*, 12393–12400.
[87] Chen, Y. Y.; Chen, D. D.; Li, Z.; Peng, X. G. Symmetry-Breaking for Formation of Rectangular CdSe two-dimensional nanocrystals in zinc-blende structure. *J. Am. Chem. Soc.* **2017**, *139*, 10009–10019.
[88] Christodoulou, S.; Climente, J. I.; Planelles, J.; Brescia, R.; Prato, M.; Martín-Garciá, B.; Khan, A. H.; Moreels, I. Chloride-induced thickness control in CdSe nanoplatelets. *Nano Lett.* **2018**, *18*, 6248–6254.
[89] Knüsel, P. N.; Riedinger, A.; Rossinelli, A. A.; Ott, F. D.; Mule, A. S.; Norris, D. J. Experimental evidence for two-dimensional ostwald ripening in semiconductor nanoplatelets. *Chem. Mater.* **2020**, *32*, 3312–3319.
[90] Ott, F. D.; Riedinger, A.; Ochsenbein, D. R.; Knüsel, P. N.; Erwin, S. C.; Mazzotti, M.; Norris, D. J. Ripening of semiconductor nanoplatelets. *Nano Lett.* **2017**, *17*, 6870–6877.
[91] Riedinger, A.; Mule, A. S.; Knüsel, P. N.; Ott, F. D.; Rossinelli, A. A.; Norris, D. J. Identifying reactive organo-selenium precursors in the synthesis of CdSe nanoplatelets. *Chem. Commun.* **2018**, *54*, 11789–11792.

[92] Bertrand, G. H. V.; Polovitsyn, A.; Christodoulou, S.; Khan, A. H.; Moreels, I. Shape control of zincblende CdSe nanoplatelets. *Chem. Commun.* **2016**, *52*, 11975–11978.

[93] Yoon, D. E.; Lee, J.; Yeo, H.; Ryou, J.; Lee, Y. K.; Kim, Y. H.; Lee, D. C. Atomistics of asymmetric lateral growth of colloidal zincblende CdSe nanoplatelets. *Chem. Mater.* **2021**, *33*, 4813–4820.

[94] Bose, S.; Song, Z. G.; Fan, W. J.; Zhang, D. H. Effect of lateral size and thickness on the electronic structure and optical properties of quasi two-dimensional CdSe and CdS nanoplatelets. *J. Appl. Phys.* **2016**, *119*, 143107.

[95] Achtstein, A. W.; Antanovich, A.; Prudnikau, A.; Scott, R.; Woggon, U.; Artemyev, M. Linear absorption in CdSe nanoplates: Thickness and lateral size dependency of the intrinsic absorption. *J. Phys. Chem. C* **2015**, *119*, 20156–20161.

[96] Yao, Y. G.; Bao, X. T.; Zhu, Y. K.; Sui, X.; Hu, A.; Bai, P.; Wang, S. F.; Yang, H.; Liu, X. F.; Gao, Y. N. Lateral quantum confinement regulates charge carrier transfer and biexciton interaction in CdSe/CdSeS core/crown nanoplatelets. *Nano Res.* **2023**, *16*, 10420–10428.

[97] Schlenskaya, N. N.; Yao, Y. Z.; Mano, T.; Kuroda, T.; Garshev, A. V.; Kozlovskii, V. F.; Gaskov, A. M.; Vasiliev, R. B.; Sakoda, K. Scroll-like alloyed CdS_xSe_{1-x} nanoplatelets: Facile synthesis and detailed analysis of tunable optical properties. *Chem. Mater.* **2017**, *29*, 579–586.

[98] Geiregat, P.; Tomar, R.; Chen, K.; Singh, S.; Hodgkiss, J. M.; Hens, Z. Thermodynamic equilibrium between excitons and excitonic molecules dictates optical gain in colloidal CdSe quantum wells. *J. Phys. Chem. Lett.* **2019**, *10*, 3637–3644.

[99] Li, Q. Y.; Lian, T. Q. A model for optical gain in colloidal nanoplatelets. *Chem. Sci.* **2018**, *9*, 728–734.

[100] Tessier, M. D.; Spinicelli, P.; Dupont, D.; Patriarche, G.; Ithurria, S.; Dubertret, B. Efficient exciton concentrators built from colloidal core/crown CdSe/CdS semiconductor nanoplatelets. *Nano Lett.* **2014**, *14*, 207–213.

[101] Leemans, J.; Singh, S.; Li, C.; Ten Brinck, S.; Bals, S.; Infante, I.; Moreels, I.; Hens, Z. Near-edge ligand stripping and robust radiative exciton recombination in CdSe/CdS core/crown nanoplatelets. *J. Phys. Chem. Lett.* **2020**, *11*, 3339–3344.

[102] Kelestemur, Y.; Guzelturk, B.; Erdem, O.; Olutas, M.; Gungor, K.; Demir, H. V. Platelet-in-box colloidal quantum wells: CdSe/CdS@CdS core/crown@shell heteronanoplatelets. *Adv. Funct. Mater.* **2016**, *26*, 3570–3579.

[103] Hu, A.; Bai, P.; Zhu, Y. K.; Song, Z. G.; Wang, R. T.; Zheng, J. C.; Yao, Y. G.; Zhang, Q.; Ding, Z. P.; Gao, P. et al. Green CdSe/CdSeS core/alloyed-crown nanoplatelets achieve unity photoluminescence quantum yield over a broad emission range. *Adv. Opt. Mater.* **2022**, *10*, 2200469.

[104] Ithurria, S.; Talapin, D. V. Colloidal atomic layer deposition (c-ALD) using self-limiting reactions at nanocrystal surface coupled to phase transfer between polar and nonpolar media. *J. Am. Chem. Soc.* **2012**, *134*, 18585–18590.

[105] Hazarika, A.; Fedin, I.; Hong, L.; Guo, J. L.; Srivastava, V.; Cho, W.; Coropceanu, I.; Portner, J.; Diroll, B. T.; Philbin, J. P. et al. Colloidal atomic layer deposition with stationary reactant phases enables precise synthesis of "digital" II-VI nano-heterostructures with exquisite control of confinement and strain. *J. Am. Chem. Soc.* **2019**, *141*, 13487–13496.

[106] Altintas, Y.; Quliyeva, U.; Gungor, K.; Erdem, O.; Kelestemur, Y.; Mutlugun, E.; Kovalenko, M. V.; Demir, H. V. Highly stable, near-unity efficiency atomically flat semiconductor nanocrystals of CdSe/ZnS hetero-nanoplatelets enabled by ZnS-shell hot-injection growth. *Small* **2019**, *15*, 1804854.

[107] Rossinelli, A. A.; Rojo, H.; Mule, A. S.; Aellen, M.; Cocina, A.; De Leo, E.; Schäublin, R.; Norris, D. J. Compositional grading for efficient and narrowband emission in CdSe-based core/shell nanoplatelets. *Chem. Mater.* **2019**, *31*, 9567–9578.

[108] Yoon, D. E.; Yeo, S.; Lee, H.; Cho, H.; Wang, N. F.; Kim, G. M.; Bae, W. K.; Lee, Y. K.; Park, Y. S.; Lee, D. C. Pushing the emission envelope for full-color realization of colloidal semiconductor core/shell nanoplatelets. *Chem. Mater.* **2022**, *34*, 9190–9199.

[109] Rossinelli, A. A.; Riedinger, A.; Marqués-Gallego, P.; Knüsel, P. N.; Antolinez, F. V.; Norris, D. J. High-temperature growth of thick-shell CdSe/CdS core/shell nanoplatelets. *Chem. Commun.* **2017**, *53*, 9938–9941.

[110] İzmir, M.; Sharma, A.; Shendre, S.; Durmusoglu, E. G.; Sharma, V. K.; Shabani, F.; Baruj, H. D.; Delikanli, S.; Sharma, M.; Demir, H. V. Blue-emitting CdSe nanoplatelets enabled by sulfur-alloyed heterostructures for light-emitting diodes with low turn-on voltage. *ACS Appl. Nano Mater.* **2022**, *5*, 1367–1376.

[111] Gao, Y. N.; Weidman, M. C.; Tisdale, W. A. CdSe nanoplatelet films with controlled orientation of their transition dipole moment. *Nano Lett.* **2017**, *17*, 3837–3843.

[112] Momper, R.; Zhang, H.; Chen, S.; Halim, H.; Johannes, E.; Yordanov, S.; Braga, D.; Blülle, B.; Doblas, D.; Kraus, T. et al. Kinetic control over self-assembly of semiconductor nanoplatelets. *Nano Lett.* **2020**, *6*, 4102–4110.

[113] Erdem, O.; Foroutan, S.; Gheshlaghi, N.; Guzelturk, B.; Altintas, Y.; Demir, H. V. Thickness-tunable self-assembled colloidal nanoplatelet films enable ultrathin optical gain media. *Nano Lett.* **2020**, *20*, 6459–6465.

[114] Bai, P.; Hu, A.; Liu, Y.; Jin, Y. Z.; Gao, Y. N. Printing and *in situ* assembly of CdSe/CdS nanoplatelets as uniform films with unity in-plane transition dipole moment. *J. Phys. Chem. Lett.* **2020**, *11*, 4524–4529.

[115] Petersen, N.; Girard, M.; Riedinger, A.; Valsson, O. The crucial role of solvation forces in the steric stabilization of nanoplatelets. *Nano Lett.* **2022**, *22*, 9847–9853.

[116] De Trizio, L.; Manna, L. Forging colloidal nanostructures via cation exchange reactions. *Chem. Rev.* **2016**, *116*, 10852–10887.

[117] Shen, Y. T.; Liang, L. J.; Zhang, S. Q.; Huang, D. S.; Zhang, J.; Xu, S. P.; Liang, C. Y.; Xu, W. Q. Organelle-targeting surface-enhanced Raman scattering (SERS) nanosensors for subcellular pH sensing. *Nanoscale* **2018**, *10*, 1622–1630.

[118] Bi, Y. H.; Cao, S.; Yu, P.; Du, Z. T.; Wang, Y. J.; Zheng, J. J.; Zou, B. S.; Zhao, J. L. Reducing emission linewidth of pure-blue ZnSeTe quantum dots through shell engineering toward high color purity light-emitting diodes. *Small* **2023**, *19*, 2303247.

[119] Li, Y.; Hou, X. Q.; Dai, X. L.; Yao, Z. L.; Lv, L. L.; Jin, Y. Z.; Peng, X. G. Stoichiometry-controlled InP-based quantum dots: Synthesis, photoluminescence, and electroluminescence. *J. Am. Chem. Soc.* **2019**, *141*, 6448–6452.

[120] Dai, L. W.; Lesyuk, R.; Karpulevich, A.; Torche, A.; Bester, G.; Klinke, C. From wurtzite nanoplatelets to zinc blende nanorods: Simultaneous control of shape and phase in ultrathin ZnS nanocrystals. *J. Phys. Chem. Lett.* **2019**, *10*, 3828–3835.

[121] Dai, L. W.; Strelow, C.; Kipp, T.; Mews, A.; Benkenstein, I.; Eifler, D.; Vuong, T. H.; Rabeah, J.; McGettrick, J.; Lesyuk, R. et al. Colloidal manganese-doped ZnS nanoplatelets and their optical properties. *Chem. Mater.* **2021**, *33*, 275–284.

[122] Dai, L. W.; Torche, A.; Strelow, C.; Kipp, T.; Vuong, T. H.; Rabeah, J.; Oldenburg, K.; Bester, G.; Mews, A.; Klinke, C. et al. Role of magnetic coupling in photoluminescence kinetics of Mn^{2+}-doped ZnS nanoplatelets. *ACS Appl. Mater. Interfaces* **2022**, *14*, 18806–18815.

[123] Basalaeva, L. S.; Grafova, V. P.; Duda, T. A.; Kurus, N. N.; Vasiliev, R. B.; Milekhin, A. G. Phonons of atomically thin ZnSe nanoplatelets grown by the colloidal method. *J. Phys. Chem. C* **2023**, *127*, 13112–13119.

[124] Wang, F.; Zhang, M. Y.; Chen, W.; Javaid, S.; Yang, H.; Wang, S.; Yang, X. Y.; Zhang, L. C.; Buntine, M. A.; Li, C. S. et al. Atomically thin heavy-metal-free ZnTe nanoplatelets formed from magic-size nanoclusters. *Nanoscale Adv.* **2020**, *2*, 3316–3322.

[125] Dai, L. W.; Strelow, C.; Lesyuk, R.; Klinke, C.; Kipp, T.; Mews, A. Mn^{2+}-doped ZnSe/ZnS core/shell nanoplatelets as low-toxic UV-to-vis light-converters with enhanced optical properties. *ACS Appl. Nano Mater.* **2023**, *6*, 11124–11134.

[126] Karan, N. S.; Sarkar, S.; Sarma, D. D.; Kundu, P.; Ravishankar, N.; Pradhan, N. Thermally controlled cyclic insertion/ejection of dopant ions and reversible zinc blende/wurtzite phase changes in ZnS nanostructures. *J. Am. Chem. Soc.* **2011**, *133*, 1666–1669.

[127] Bouet, C.; Laufer, D.; Mahler, B.; Nadal, B.; Heuclin, H.; Pedetti, S.; Patriarche, G.; Dubertret, B. Synthesis of zinc and lead chalcogenide core and core/shell nanoplatelets using sequential cation exchange reactions. *Chem. Mater.* **2014**, *26*, 3002–3008.

[128] Es, M. S.; Colak, E.; Irfanoglu, A.; Kelestemur, Y. Direct synthesis of zinc-blende ZnSe nanoplatelets. *ACS Omega* **2024**, *9*, 27438–27445.

[129] Huang, B.; Huang, Y. H.; Zhang, H. C.; Lu, X. M.; Gao, X. M.; Zhuang, S. L. Electrochemical control over the optical properties of II-VI colloidal nanoplatelets by tailoring the station of extra charge carriers. *ACS Appl. Mater. Interfaces* **2023**, *15*, 21354–21363.

[130] Ashokan, A.; Han, J.; Hutchison, J. A.; Mulvaney, P. Spectroelectrochemistry of CdSe/$Cd_xZn_{1-x}S$ nanoplatelets. *ACS Nano* **2023**, *17*, 1247–1254.

[131] Dede, D.; Taghipour, N.; Quliyeva, U.; Sak, M.; Kelestemur, Y.; Gungor, K.; Demir, H. V. Highly stable multicrown heterostructures of type-II nanoplatelets for ultralow threshold optical gain. *Chem. Mater.* **2019**, *31*, 1818–1826.

[132] Geuchies, J. J.; Dijkhuizen, R.; Koel, M.; Grimaldi, G.; du Fossé, I.; Evers, W. H.; Hens, Z.; Houtepen, A. J. Zero-threshold optical gain in electrochemically doped nanoplatelets and the physics behind it. *ACS Nano* **2022**, *16*, 18777–18788.